

Magnetotransport of functional oxide heterostructures affected by spin-orbit coupling: a tale of two-dimensional systems

Robert Bartel, Elias Lettl, Patrick Seiler, Thilo Kopp, German Hammerl

Angaben zur Veröffentlichung / Publication details:

Bartel, Robert, Elias Lettl, Patrick Seiler, Thilo Kopp, and German Hammerl. 2022. "Magnetotransport of functional oxide heterostructures affected by spin-orbit coupling: a tale of two-dimensional systems." *physica status solidi (b)* 259 (5): 2100154. <https://doi.org/10.1002/pssb.202100154>.

Magnetotransport of Functional Oxide Heterostructures Affected by Spin–Orbit Coupling: A Tale of Two-Dimensional Systems

Robert Bartel, Elias Lettl, Patrick Seiler, Thilo Kopp, and German Hammerl*

Oxide heterostructures allow for detailed studies of 2D electronic transport phenomena. Herein, different facets of magnetotransport in selected spin–orbit-coupled systems are analyzed and characterized by their single-band and multiband behavior, respectively. Experimentally, temperature and magnetic field dependent measurements in the single-band system $\text{BaPbO}_3/\text{SrTiO}_3$ reveal strong interplay of weak antilocalization (WAL) and electron–electron interaction (EEI). Within a scheme which treats both, WAL and EEI, on an equal footing a strong contribution of EEI at low temperatures is found which suggests the emergence of a strongly correlated ground state. Furthermore, now considering multiband effects as they appear, e.g., in the model system $\text{LaAlO}_3/\text{SrTiO}_3$, theoretical investigations predict a huge impact of filling on the topological Hall effect in systems with intermingled bands. Already weak band coupling produces striking deviations from the well-known Hall conductivity that are explainable in a fully quantum mechanical treatment which builds upon the hybridization of intersecting Hofstadter bands.


1. Introduction

Perovskite-related oxides show a huge variety of intrinsic properties.^[1] With oxide heterostructures, it is not only possible to combine such material characteristics but also to identify novel electronic phases emerging on the nanoscale which allows to trigger a plethora of functionalities.^[2,3] At the interfaces of certain polar insulators confined metallic electronic systems appear driven by electronic reconstruction.^[4,5] In addition, inversion symmetry is systemically broken, a key ingredient for strong Rashba-type spin–orbit coupling, leading to anomalous transport

properties which will be addressed in this article. Moreover, such electronic systems, when gapped, may assume nontrivial values of topological invariants causing a particular behavior of their magnetotransport. In fact, magnetotransport allows to obtain a fingerprint of the electronic state of metals, especially also of oxide heterostructures with their complex electronic properties controlled by sizable spin–orbit coupling, multiband behavior, disorder, and Coulomb interaction.

This article covers two complementary spin–orbit-coupled electronic systems, both with regard to magnetotransport: a disordered and a defect-free 2D system. Correspondingly, the article is organized as follows: in Section 2, we examine experimentally BaPbO_3 thin films grown on SrTiO_3 . The perovskite-related oxide BaPbO_3 is a single-band metal. In this system with Rashba spin–orbit coupling disorder accounts for weak antilocalization (WAL) in the presence of electron–electron interaction (EEI). We briefly introduce these theoretical concepts of quantum corrections to transport properties before we analyze our temperature- and magnetic field-dependent measurements. We then self-consistently extract parameters describing spin–orbit coupling and EEI—indicating a correlated ground state in BaPbO_3 . In a further step toward a general understanding it suggests itself to consider the spin–orbit coupling dominated magnetotransport beyond the single-band 2D systems. In Section 3, we analyze the influence of magnetic fields on the transport properties of a defect-free 2D multiband system in the fully quantum mechanical treatment of linear response theory. Our work is inspired by the fact that magnetotransport studies of $\text{LaAlO}_3/\text{SrTiO}_3$ interfaces under applied hydrostatic pressure can lead to counterintuitive results if evaluated with standard semiclassical techniques.^[6] However, as the semiclassical Boltzmann transport theory builds upon a single-band model its validity in case of multiband systems like $\text{LaAlO}_3/\text{SrTiO}_3$ should be questioned.^[7] This is especially true if one expects topological band aspects to play a fundamental role. After a general model description, we start by analyzing magnetotransport for the single-band case revisiting the results of the Hofstadter model. In a next step, we discuss multiband behavior affected by atomic or Rashba-type spin–orbit coupling.

R. Bartel, E. Lettl, P. Seiler, T. Kopp, G. Hammerl
Center for Electronic Correlations and Magnetism
Experimental Physics VI
Institute of Physics
University of Augsburg
86135 Augsburg, Germany
E-mail: german.hammerl@physik.uni-augsburg.de

 The ORCID identification number(s) for the author(s) of this article can be found under <https://doi.org/10.1002/pssb.202100154>.

© 2021 The Authors. physica status solidi (b) basic solid state physics published by Wiley-VCH GmbH. This is an open access article under the terms of the Creative Commons Attribution License, which permits use, distribution and reproduction in any medium, provided the original work is properly cited.

DOI: 10.1002/pssb.202100154

2. Magnetotransport in Single-Band Systems Governed by Disorder

Recently, we found that BaPbO₃ thin films grown on (001)-oriented SrTiO₃ single crystals show single-band behavior and a pronounced magnetoresistance (MR) which at low magnetic fields is evidently ruled by WAL.^[8] Surprisingly, temperature-dependent measurements of the sheet resistance $R_{\square}(T)$ account for an insulating low-temperature state, contradicting the WAL result of magnetoconductance. Such a counterintuitive behavior of thin film samples was observed before.^[9,10] It is argued that MR and $R_{\square}(T)$ may originate from distinct sensitive channels leading to different measurement-dependent ground states.^[9–12] By carefully investigating MR and $R_{\square}(T)$, we unveiled that the expected WAL contribution in $R_{\square}(T)$ is covered by a pronounced EEI contribution. However, up to now, we neglected the mutual effect of EEI to MR as we considered it to be small.

Before we examine the influence of EEI on the WAL signal in our samples, let us discuss the generic temperature and magnetic field dependencies on the quantum corrections of the electrical transport of a disordered 2D system.

Due to weak disorder low-temperature electronic transport in 2D materials is affected by quantum interference (QI) resulting either in insulating or metallic ground states. QI contributes significantly to the electrical transport only if the electrons' temperature-dependent dephasing time τ_{ϕ} is large compared with, e.g., the elastic scattering time τ_e : randomly scattered electrons will unavoidably self-interfere constructively with their time-reversal counterparts leading to WL with its insulating ground state.^[13–17] Pronounced spin–orbit (SO) coupling described by a timescale τ_{so} associated with the D'yakonov–Perel' spin relaxation ($\tau_{so} \ll \tau_{\phi}$) instead contributes an additional phase causing WAL which induces a metallic ground state.^[15,18–20]

Both QI effects, WL and WAL, are characteristically influenced by applied time-reversal symmetry-breaking external magnetic fields which makes it possible to experimentally decide on the type of quantum corrections. A comprehensive description of the magnetic field-dependent first-order quantum correction to the conductivity of an ideal 2D material is given by the well-accepted Iordanskii–Lyanda-Geller–Pikus theory which relates the specific magnetic field dependence to the winding number of the spin expectation value around the Fermi surface.^[19,21,22] In case of triple spin winding, found in, e.g., SrTiO₃-based 2D thin films,^[23–25] the Iordanskii–Lyanda-Geller–Pikus theory merges to the analytical result of the Hikami–Nagaoka–Larkin theory.^[15] The first-order quantum correction to the conductivity σ in applied magnetic field B triggered by QI can then be expressed as

$$\delta\sigma^{QI}(B) = \frac{e^2}{\pi h} \left[\Psi\left(\frac{1}{2} + \frac{B_{so} + B_{\phi}}{B}\right) - \frac{1}{2}\Psi\left(\frac{1}{2} + \frac{B_{\phi}}{B}\right) + \frac{1}{2}\Psi\left(\frac{1}{2} + \frac{2B_{so} + B_{\phi}}{B}\right) - \Psi\left(\frac{1}{2} + \frac{B_e}{B}\right) \right] \quad (1)$$

with Ψ being the digamma function.^[26] The introduced effective magnetic fields are related to the scattering times via

$$B_{e/\phi/so} = \frac{\hbar}{4eD\tau_{e/\phi/so}} \quad (2)$$

with D being the diffusion constant.

Magnetoconductivity in relevant magnetic fields $B \ll B_e$ is then given by

$$\Delta\sigma^{QI}(B) = \delta\sigma^{QI}(B) - \delta\sigma^{QI}(0) = \frac{e^2}{\pi h} \left[\Psi\left(\frac{B}{B_{so} + B_{\phi}}\right) - \frac{1}{2}\Psi\left(\frac{B}{B_{\phi}}\right) + \frac{1}{2}\Psi\left(\frac{B}{2B_{so} + B_{\phi}}\right) \right] \quad (3)$$

where $\Psi(x) = \ln(x) + \psi\left(\frac{1}{2} + \frac{1}{x}\right)$.

In the 2D case, experimental data are often presented in terms of the related MR calculated from the magnetic field-dependent resistance $R(B)$ via

$$MR = \frac{R(B) - R(0)}{R(0)} = \frac{1}{1 + \rho(0)\Delta\sigma^{QI}(B)} - 1 \quad (4)$$

where the 2D resistivity ρ is identified with the sheet resistance $R_{\square} = \frac{w}{l} \cdot R$ with l and w being the measurement bar's length and width, respectively.

To compare the conductivity influenced either by magnetic fields or temperature, Equation (1) can be further adapted: Evaluating $\delta\sigma^{QI}(B)$ in the limit of zero magnetic field the first-order correction to the conductivity can be individually expressed for both low-temperature states associated with WL and WAL, respectively: in case of $\tau_{so} \gg \tau_{\phi}$ ($B_{so} \ll B_{\phi}$) Equation (1) treats WL and simplifies to

$$\delta\sigma^{WL}(B \rightarrow 0) = \frac{e^2}{\pi h} \ln\left(\frac{B_{\phi}}{B_e}\right) \quad (5)$$

whereas in case of $\tau_{so} \ll \tau_{\phi}$ ($B_{so} \gg B_{\phi}$) it relates to WAL and reads

$$\delta\sigma^{WAL}(B \rightarrow 0) = -\frac{1}{2} \frac{e^2}{\pi h} \ln\left(\frac{B_e^2 B_{\phi}}{2B_{so}^3}\right) \quad (6)$$

B_{ϕ} is controlled by inelastic scattering and an algebraic temperature dependence of B_{ϕ} is assumed by

$$B_{\phi}(T) = \gamma + \beta T^{\alpha} \quad (7)$$

with β being a scaling factor, γ modeling a saturation in dephasing at zero temperature, and α being an exponent in the range between 1 and 2 combining contributions of both electron–phonon and electron–electron scattering.^[27,28]

With the help of Equation (7), the first-order quantum corrections to the conductivity become temperature-dependent with an insulating state in case of WL

$$\delta\sigma^{WL}(T) = \frac{e^2}{\pi h} \ln\left(\frac{\gamma + \beta T^{\alpha}}{C^{WL}}\right) \quad (8)$$

and with a metallic state in case of WAL

$$\delta\sigma^{\text{WAL}}(T) = -\frac{1}{2\pi h} \ln\left(\frac{\gamma + \beta T^\alpha}{C^{\text{WAL}}}\right) \quad (9)$$

Both progressions are exclusively driven by the temperature dependence of the dephasing scattering with C^{WL} and C^{WAL} being temperature-independent constants determined by WL and WAL, respectively.

An insulating ground state is not necessarily induced by Anderson localization but can also be incited by EEI.^[16,17,29] In 2D systems, the conductivity correction due to EEI reveals nearly the same logarithmic temperature dependence compared with WL

$$\delta\sigma^{\text{EEI}}(T) = \frac{e^2}{\pi h} \ln\left(\frac{T^\zeta}{C^{\text{EEI}}}\right) \quad (10)$$

with ζ being an exponent related to screening effects and ranging between 0.35 for no screening and 1 for perfect screening, and C^{EEI} being a temperature-independent constant defined by EEI. The temperature dependence can again be compared with magnetic field-dependent measurements as in the presence of magnetic fields a finite Zeeman splitting (ZS) is responsible for a sizable magnetoconductivity in 2D systems^[17]

$$\Delta\sigma^{\text{ZS}}(\tilde{B}(T)) = -\frac{e^2}{\pi h} \frac{2(1-\zeta)}{3} g_{2D}(\tilde{B}(T)) \quad (11)$$

with $\tilde{B}(T) = (g\mu_B B)/(k_B T)$, g the Landé factor, and g_{2D} a function defined by

$$g_{2D}(\tilde{B}(T)) = \int_0^\infty d\Omega \ln\left|1 - \frac{\tilde{B}(T)^2}{\Omega^2}\right| \frac{d^2}{d\Omega^2} \frac{\Omega}{\exp(\Omega) - 1} \quad (12)$$

which can be evaluated numerically.

2.1. Sample Growth and Characterization of BaPbO₃ Thin Films

All samples discussed were grown by pulsed laser deposition (PLD). The PLD system uses a KrF excimer laser with a wavelength of 248 nm and a nominal fluency of 2 J cm⁻². The used polycrystalline BaPbO₃ targets were obtained commercially with asked maximum achievable density. They are evaluated to have purities of at least 99.95%. Prior to each sample growth the surface of the targets were carefully cleaned.

BaPbO₃ thin films were grown on commercially available, one-side polished, (001)-oriented single-crystalline SrTiO₃ substrates with a given size of 5 × 5 × 1 mm³. To obtain defined BaPbO₃/SrTiO₃ interfaces the substrates were either TiO₂ terminated using a hydrogen fluoride (HF) buffer solution^[30,31] and subsequently annealed in pure oxygen flow at about 950 °C for 7 h or cleansed by lens paper as well as ultrasonic bath treatment in acetone and isopropyl.

The substrates were then fixed for either infrared laser heating or resistive heating on appropriate platforms using silver paste and transferred via a load-lock system and transfer chamber into permanently air-sealed PLD vacuum chambers. Depending on the pretreatment the substrates were either slowly heated to nominally 554 °C during at least 60 min in case

of HF-treated substrates or heated up to 800 °C within a few minutes for at least 5 min in case of cleansed substrates to purify the substrate surface and then reheated to about 554 °C within seconds, both in a pure oxygen background pressure of about 1 mbar.

Thin-film deposition was done using a nominal laser pulse energy of 550 and 650 mJ—depending on the used PLD chamber—at a laser frequency of 5 Hz. The number of laser pulses was chosen individually resulting in desired thin-film thicknesses. With this setup, the growth rate of BaPbO₃ was determined to be about 0.34 nm per laser pulse.

After thin-film deposition, the vacuum chamber was immediately filled with pure oxygen to at least 400 mbar, whereas the sample was cooled to about 400 °C within 3 min and kept at that temperature for additional 17 min for annealing. Then the sample was allowed to freely cool-down to room temperature before the chamber was evacuated again for unloading the sample.

Film thicknesses were routinely obtained by X-ray reflectivity (XRR). Conducted XRR fits resulted in averaged surface and interface roughness better than 0.6 and 0.7 nm, respectively. X-ray diffraction (XRD) measurements indicate that all epitaxial BaPbO₃ layers are (001)-oriented.

All samples were patterned into four-probe and Hall bar layouts using a standard photolithography system (mercury arc lamp) followed-up by ion-milling. To minimize contact resistances gold was sputtered onto the contact pads. All samples were electrically contacted using copper wires (0.1 mm in diameter) soldered to the puck and glued via silver paste to the samples.

All electrical transport measurements were carried out using a commercial 14-T physical property measurement system (PPMS) with an electrical transport option (ETO). The applied AC currents were in the range of 0.1–1 μA with typical frequencies from 70 to 128 Hz.

2.2. Experimental Results and Discussion

In this article, we account for the EEI contribution intrinsically involved in the MR data. Assuming both WAL and EEI contributing equally via Equation (3) and (11), we self-consistently evaluate MR and $R_{\square}(T)$ within the following iterative scheme:

We start by applying Equation (3) to our raw MR data and extract the WAL contribution neglecting any EEI contribution during the first iteration. Subsequently, with the help of Equation (9), we are able to subtract the WAL contribution to reveal the pure temperature-dependent sheet resistance due to EEI which then provides a value of the screening factor ζ . By accounting for a pronounced Zeeman splitting the MR data can now be reevaluated again allowing for a priorly hidden EEI contribution that is described by Equation (11) with a presumed Landé factor $g = 2$. We carry out this procedure successively until the screening factor ζ settles to a constant value. To avoid oscillations which may prevent convergence—as ζ is close and limited to 1—we average the obtained ζ values within the last three iterations.

Exemplarily the result of such a self-consistent evaluation of MR and $R_{\square}(T)$ in terms of WAL and EEI are shown in **Figure 1** and **2**. Figure 1 shows temperature-dependent MR data taken from a 15.0 nm-thick BaPbO₃ thin film showing an increase in MR to a maximum value at a magnetic field of

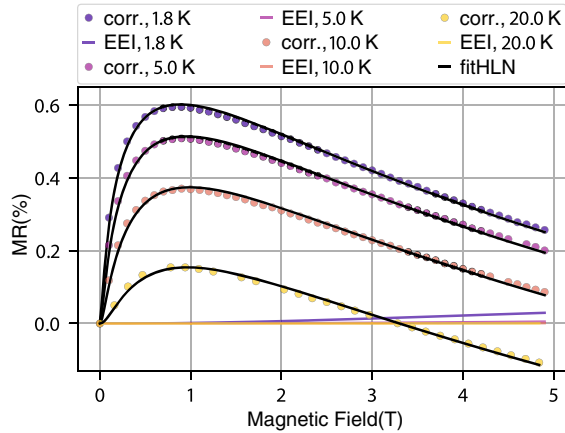


Figure 1. Reevaluated MR data taken at different temperatures of a 15.0 nm thick BaPbO₃ thin film grown on a (001)-oriented single-crystalline SrTiO₃ substrate. The symmetrized raw data were self-consistently corrected from EEI contributions (Equation (11)) with the presumed value of $g = 2$ and $\zeta = 0.91$ retrieved from analysis of the $R_{\square}(T)$ measurement (see Figure 2). The EEI contribution for each temperature is plotted as a solid line with its corresponding color. Black solid lines show best fits (least squares method) of the EEI-corrected MR data (see “corr.,” i.e., colored dots) using Equation (3) resulting in an averaged value of $B_{s0} \approx 0.22$ T. The obtained temperature dependence of B_{ϕ} can be described by an algebraic dependence (Equation (7)) with $\alpha = 1.99$, $\beta = 0.14$ mT K^{- α} , and $\gamma = 7.50$ mT (not shown) determining the WAL correction in the $R_{\square}(T)$ analysis (see Figure 2).

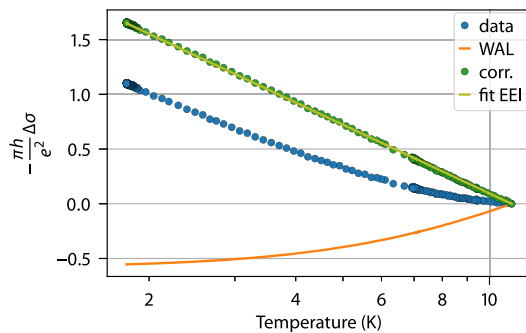


Figure 2. Progression of the change in conductivity referenced to the temperature $T_{ref} = 11.1$ K in logarithmic scale. Blue dots show original measured data, whereas the expected progression for WAL is plotted in orange, retrieved from MR analysis (see Figure 1) following Equation (9) indicating a metallic low-temperature state. In green, WAL-revised data are shown which are perfectly explained by the EEI contribution solely (Equation (10))—resulting in $\zeta = 0.91$.

$B \approx 0.85$ T with a following decrease at higher magnetic fields, confirming our former results.^[8] The MR data were corrected from concomitant EEI by subtracting its contribution via Equation (11) with $\zeta = 0.91$ retrieved from $R_{\square}(T)$ analysis. As expected, EEI contributes only slightly (see colored lines in Figure 1). The re-evaluated MR data can now be perfectly fitted in terms of WAL using Equation (3).

Further, the fits result in an averaged $B_{s0} \approx 0.22$ T and a temperature dependence of B_{ϕ} that can be best described with

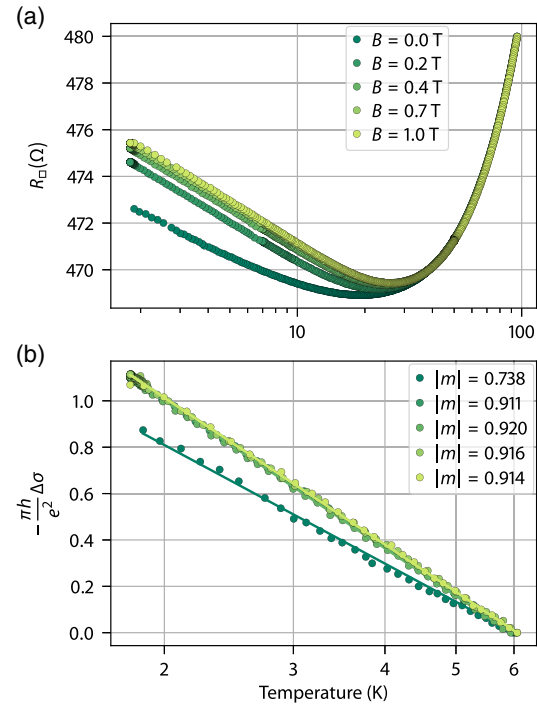


Figure 3. Progressions of $R_{\square}(T)$ as well as changes in conductivity normalized to $T_{ref} = 6$ K while applying various perpendicular magnetic fields between 0.2 and 1 T (in logarithmic scale). The magnetic field suppresses WAL contributions, whereas EEI contributions are unaffected. The slopes clearly show trends toward an insulating ground state as the magnetic field increases. The gradient $|m|$ was linearly fitted, representing ζ in case of suppressed WAL. The resulting ζ ranging between 0.91 and 0.92 is in good agreement with the prior self-consistent analysis ($\zeta = 0.91$).

$\alpha = 1.99$ following Equation (7) supporting a dephasing mechanism mainly due to electron–phonon scattering.

Simultaneously taken $R_{\square}(T)$ data are likewise affected by EEI at low temperature, see zero-field data in Figure 3: Upon cooling starting from room temperature R_{\square} steadily decreases, then reaches a minimum at about 11.1 K and subsequently rises again. The high-temperature progression can be well understood in terms of electron–phonon scattering as well as thermally activated dislocation scattering.^[32]

The low-temperature behavior is unequivocally controlled by quantum corrections. Figure 2 shows the change of the conductivity

$$\Delta\sigma = \left(\frac{1}{\rho(T)} - \frac{1}{\rho(T_{ref})} \right) \quad (13)$$

normalized to $T_{ref} = 11.1$ K. The measured data were re-evaluated by subtracting the influence of WAL following Equation (9) with parameters acquired from evaluations of the MR. The corrected data show a clear logarithmic increase perfectly described by EEI following Equation (10) that results in $\zeta = 0.91$.

For consistency, we applied the just established self-consistent calculations of B_{s0} and ζ to the data presented in the study by

Seiler et al.,^[8] comparing different sample thicknesses: For the sample with thickness 21.3 nm, the WAL contribution expressed by B_{so} changes in its average value from 0.10 to 0.13 T, whereas EEI represented by ζ remains unchanged at a value of 0.97. The 4.8 nm thick sample shows a small increase in B_{so} from 0.23 to 0.24 T in average, whereas ζ changes from 0.84 to 0.89. It will be interesting to further study the thickness dependence on both the WAL and EEI contributions.

An independent approach to extract the EEI contribution without being affected by WAL is the magnetic field dependence of $R_{\square}(T)$. Magnetic fields $B > B_{\phi}$ cause the quantum corrections induced by QI ($\delta\sigma_B^{QI}$) to become temperature independent^[33] and therefore to vanish by evaluating

$$\Delta\sigma_B^{QI}(T) = \delta\sigma_B^{QI}(T) - \delta\sigma_B^{QI}(T_{ref}) \quad (14)$$

Hence, in the presence of even small magnetic fields, the temperature dependence of the conductance below T_{ref} should be solely reigned by EEI.

In Figure 3, the temperature-dependent progression of $R_{\square}(T)$ as well as $\Delta\sigma(T)$ normalized to now $T_{ref} = 6$ K are plotted, both in logarithmic scale. The magnetic field further increases R_{\square} pronouncing the insulating ground state according to the expected suppression of WAL effects. The gradient $|m|$ (which translates directly into the value of ζ in case of suppressed WAL) extracted from linear fits clearly increases and saturates at $|m| \approx 0.915$ in reasonable good agreement with our previous result ($\zeta = 0.91$).

3. Magnetotransport in Multiband Systems in the Clean Limit

Magnetotransport studies have also been carried out on multiband oxide heterostructures. For example, for the confined electronic system at the interface of $\text{LaAlO}_3/\text{SrTiO}_3$, an EEI contribution was suggested to dominate transport at low temperatures.^[32] This interpretation was challenged in a more recent WAL analysis within the framework of a semiclassical approach to multiband magnetotransport.^[6]

A fully quantum mechanical multiband treatment of WAL was established for degenerate, isotropic t_{2g} bands.^[34,35] However, for various multiband systems, such as the electron system at the $\text{LaAlO}_3/\text{SrTiO}_3$ interface, band hybridization at crossing points or rather lines is present in the relevant filling regime. This so far has not been addressed within a fully quantum mechanical approach to WAL.

Here, as a first step to a more realistic modeling, we develop a description of magnetotransport in the presence of band crossings within an effective two-band model for a defect-free lattice system. We investigate explicitly the Hall conductivity in the presence of atomic and Rashba-like spin-orbit coupling.

Before we reexamine the prerequisites of magnetotransport of a single-band model and the two-band case with its particular Hall conductivity, let us introduce the generic model description.

We use a tight-binding representation for the Hamiltonian of a noninteracting electron system in an infinite 2D crystalline lattice

$$H = \sum_{j,l} \sum_{\mu,\nu} t_{R_j-R_l}^{\mu,\nu} (c_{R_j}^{\mu})^{\dagger} c_{R_l}^{\nu} = \int_{\Omega_{BZ}} d^2k \sum_{\mu,\nu} h_k^{\mu,\nu} (c_k^{\mu})^{\dagger} c_k^{\nu} \quad (15)$$

where R_j is a lattice vector. Lowercase Greek letters μ, ν label the states within a unit cell. The integral over the lattice momenta k is taken over the first Brillouin zone (BZ), the area of which we denote by Ω_{BZ} .

The coordinate operator is assumed to be diagonal in the chosen basis $\{|R_j, \mu\rangle\}$

$$r = \sum_j \sum_{\mu} (R_j + d^{\mu}) (c_{R_j}^{\mu})^{\dagger} c_{R_j}^{\mu} = \int_{\Omega_{BZ}} d^2k \sum_{\mu} (c_k^{\mu})^{\dagger} i \nabla_k c_k^{\mu} \quad (16)$$

where d^{μ} is the position of the state μ within the unit cell. For the last equality to hold the Fourier transformation of the creation and annihilation operators must be defined for each state μ individually with respect to its exact position

$$c_k^{\mu} = \frac{1}{\sqrt{\Omega_{BZ}}} \sum_j \exp[-ik(R_j + d^{\mu})] c_{R_j}^{\mu} \quad (17)$$

Linear response theory provides us with the Kubo formula for the electric conductivity in the static limit

$$\sigma_{DC}^{\alpha\beta} = -i\hbar \lim_{\eta \rightarrow 0^+} \int_{\Omega_{BZ}} \frac{d^2k}{(2\pi)^2} \sum_{m,n} \frac{f(E_k^m) - f(E_k^n)}{E_k^m - E_k^n} \times \frac{\langle k, m | J^{\alpha} | k, n \rangle \langle k, n | J^{\beta} | k, m \rangle}{E_k^m - E_k^n + i\hbar\eta} \quad (18)$$

where $|k, m\rangle$ describes an eigenstate of the Hamiltonian in band m and E_k^m the corresponding eigenvalue.^[36–38] For numerical stability η has to be kept finite, which may be roughly interpreted as a finite scattering rate. The Fermi distribution $f(E_k^m)$ actually also depends on the chemical potential and temperature. The electric current operator J in the reciprocal basis can be written in terms of the gradient of the Hamiltonian matrix $h_k^{\mu,\nu}$

$$J = -e \frac{i}{\hbar} [H, r] = -e \int_{\Omega_{BZ}} d^2k \sum_{\mu,\nu} \left(\frac{1}{\hbar} \nabla_k h_k^{\mu,\nu} \right) (c_k^{\mu})^{\dagger} c_k^{\nu} \quad (19)$$

where e is the elementary electric charge.^[39–41]

As the coordinate operator (Equation (16)) is assumed to be diagonal, the effect of a homogeneous external magnetic field on the orbital degrees of freedom is given purely in terms of the Peierls phase.^[42,43] No further parameters enter the model description.^[44,45] In general, the Hamiltonian will then not commute with the lattice translation operators T_{R_j} , because of the real space dependence of the vector potential. For a homogeneous external magnetic field with rational flux p/q per 2D unit cell, in units of the magnetic flux quantum $\Phi_0 = h/e$, translation symmetry can be restored by introducing magnetic translation operators $T_{R_j}^M$.^[46–48] Those are a combination of a gauge transformation and a lattice translation. They do not commute with each other except if transporting a particle to the opposite corner of a parallelogram penetrated by an integer number of magnetic flux quanta. The smallest such parallelogram with a nonvanishing area is the so-called magnetic unit cell, which is a q times

enlarged version of the lattice unit cell, so that it is penetrated by an integer number p of magnetic flux quanta. Here and in the following p and q are assumed to be coprime integers.

The quantum numbers of the commuting magnetic translation operators are good quantum numbers to characterize the eigenstates of the Hamiltonian. They replace the lattice momenta of the translation invariant system, resulting again in a Hamiltonian in reciprocal space of the form of Equation (15), where μ, ν now label the states in a magnetic unit cell. From a band perspective, the enlargement of the unit cell to a magnetic one leads to a splitting of each of the initial dispersion relations without field into q magnetic Bloch bands (so-called Hofstadter bands). Each of the Hofstadter bands contains only a fraction $1/q$ of the states of the original bands.^[49]

Under applied magnetic field the matrix elements of the current operator in the eigenbasis of the Hamiltonian, as appearing in Equation (18), have the same q -fold degeneracy in the magnetic BZ as the eigenvalues.^[49] The integral over \mathbf{k} must therefore in the magnetic case only be taken over a reduced part of the magnetic BZ.^[50–52]

3.1. Anisotropic Hofstadter Model

Within this framework, we now consider a square lattice with one orbital per site and nearest-neighbor hopping only

$$H = \int_{\Omega_{\text{BZ}}} d^2\mathbf{k} [-2t_x \cos(k_x) - 2t_y \cos(k_y)] c_{\mathbf{k}}^\dagger c_{\mathbf{k}} \quad (20)$$

The lattice spacing is set to 1 and spin polarization is assumed. We note that a rectangular lattice geometry would in the following only lead to a scaling of longitudinal conductivities and densities of states. We allow for an asymmetry in the hopping strength along the two different bond directions. By introducing the Peierls phase to account for a homogeneous magnetic flux through the lattice cells, one arrives at the Harper–Hofstadter Hamiltonian.^[49,53]

To review how band structure and topology affect the conductivity of the anisotropic Hofstadter model, we first choose a flux of $p/q = 1/10$. The original cosine band is then split up into $q = 10$ separate Hofstadter bands, as long as the system is truly 2D ($t_x \neq 0 \neq t_y$). In case of q being even the two middle sub-bands in the Hofstadter model touch.^[49,54] All other bands are isolated by finite energy gaps and have a Chern number of $+1$.^[54,55] This can be verified in **Figure 4**, as the longitudinal conductivity vanishes in those gaps, whereas the transversal conductivity is quantized in units of the conduction quantum e^2/h . This holds approximately true even at finite temperatures and scattering rates, as long as temperature $k_B T$ and scattering-induced energy broadening $\hbar\eta$ are much smaller than the bandgaps. If the chemical potential on the other hand is placed within a Hofstadter band, one calculates a finite Drude weight in case of the longitudinal conductivity and the Hall signal is shifted away from its quantized values.

In the limit of a 1D system with either $t_x = 0$ or $t_y = 0$, the Peierls phase can be gauged away completely. One is left with the field-free model with a single band with zero Hall signature.

As the anisotropy between the hopping parameters in x- and y-directions is in-/decreased, only the contributions to the conductivities, which are not of topological character, approach the fully an-/isotropic limit (see yellow/orange lines in **Figure 4**). For

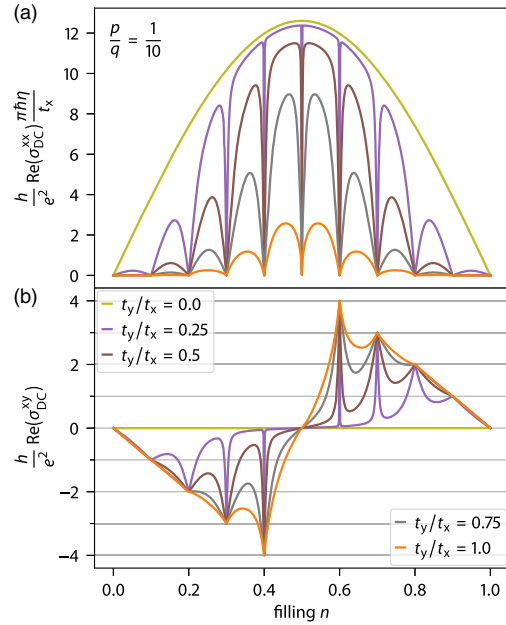


Figure 4. Quantization of conductivities: a) longitudinal and b) transversal signals for different anisotropy values in the Hofstadter model plotted versus band filling with a magnetic flux per unit cell of $p/q = 1/10$ of a magnetic flux quantum. The evaluations are done setting $k_B T = 5t_x \cdot 10^{-4}$ and $\hbar\eta = t_x \cdot 10^{-3}$. The periodicity of the field-free system is taken to be $N = 12\,000$ lattice cells in each direction.

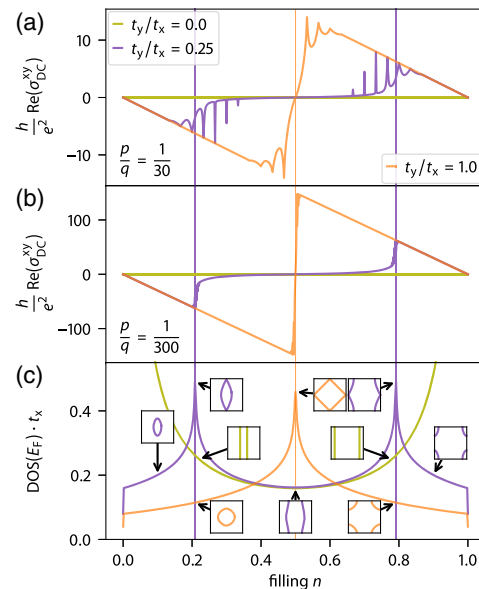


Figure 5. Hall conductivity in respect to open and closed semiclassical orbits: Hall signal for a) $p/q = 1/30$ of a flux quantum per unit cell and b) $p/q = 1/300$. All other parameters are unchanged from **Figure 4**. c) Density of states of the field-free model at the Fermi energy in dependence of the filling factor. The insets show the Fermi surfaces at certain fillings in the first BZ, where the horizontal axis represents k_x and the vertical axis k_y . In all three subfigures, the positions of the logarithmic Van Hove singularities of the model with anisotropy $t_y/t_x = 0.25$ and the isotropic case are indicated by vertical lines.

filling factors $n = r/q$, on the other hand, where r Hofstadter bands are completely filled, the conductivities are invariant as long as no single energy gap becomes too small.

By reducing the magnetic flux (**Figure 5**) for a fixed value of the anisotropy with $0 < t_y/t_x < 1$, one can see that the Hall signal is filling-wise divided into distinct regimes where it either approaches the fully anisotropic or the isotropic limit. The same holds true also for the longitudinal conductivity. The boundaries between those different cases are associated with the positions of the logarithmic Van Hove singularities of the field-free model.^[56] This is reasonable if one recalls that those two Van Hove singularities originate from the saddle points of the band structure and are thus at the same fillings as the transitions between different kinds of semiclassical orbits.^[57] In this specific case, one finds closed orbits for low and high fillings of the anisotropic Hofstadter model, whereas in between the logarithmic Van Hove singularities only open orbits exist (see insets in **Figure 5c**). The isotropic limit is a special case: the two considered Van Hove singularities merge in energy, which leads to an immediate switching from electron to hole like closed orbits, with only a single energy level in between accommodating open orbits.^[58] In the fully anisotropic limit, on the other hand, there are only open orbits, which are purely 1D and yield no Hall signal as already mentioned.

The sharp topological peaks in the regions of open orbits that one finds for high magnetic fields (**Figure 4b**) are washed out quickly with decreasing magnetic field by finite temperatures and scattering, as there the gaps between the Hofstadter bands become small.

From semiclassical Boltzmann transport theory, one can deduce an expression for the nontopological contributions to the Hall conductivity of the considered band model at zero temperature, assuming $t_y \leq t_x$

$$\sigma_{DC}^{xy} = -\frac{e^2 q}{h p} \left(n - \frac{|\bar{k}_x(n)|}{\pi} \right) \quad (21)$$

where $|\bar{k}_x(n)|$ is the absolute value of the time averaged k_x -value along a semiclassical orbit at the Fermi surface for a certain band filling n (compare previous studies^[59,60]). So in case of only closed electron orbits $|\bar{k}_x| = 0$ and in case of exclusively closed hole orbits at the Fermi level $|\bar{k}_x| = \pi$, whereas for open orbits, $|\bar{k}_x(n)|$ is bounded by the minimal and maximal absolute k_x -value of the open orbit. Thus, opposed to the standard textbook derivations, Equation (21) is not limited to the linear contributions of closed electron or hole orbits to the transversal conductivity.^[60] It describes the complete filling range, even the suppression of the Hall signal for open orbits and the switching from electron to hole like behavior at half filling.

For a similar study about open and closed orbits in the Hofstadter model where the anisotropy is due to a diatomic basis, see Göbel et al.^[56]

3.2. Effective Two-Band Model in a Perpendicular Magnetic Field

With knowledge of the magnetotransport behavior of the single-band model from Section 3.1, one can now proceed to study a

multiband system, where two such square lattice cosine bands are combined. Its field-free Hamiltonian is given by

$$H = \int_{\Omega_{BZ}} d^2k \sum_{\mu=1,2} \left\{ -2 [t_x^\mu \cos(k_x) + t_y^\mu \cos(k_y)] (c_k^\mu)^\dagger c_k^\mu + \varepsilon^\mu (c_k^\mu)^\dagger c_k^\mu + \sum_{\nu=1,2} \Delta(k_y) t_x^{\mu,\nu} (c_k^\mu)^\dagger c_k^\nu \right\} \quad (22)$$

where ε^μ allows for a relative energy shift of the two bands against each other, τ_x is the first Pauli matrix, and $\Delta(k_y)$ controls a spin-orbit-like coupling effect (see the following text). We assume that both states in a unit cell ($\mu = 1, 2$) are centered at the same point ($\mathbf{d}^1 = \mathbf{d}^2$).

To provide a specific example of a perovskite oxide, Hamiltonian (22) can accommodate each reduced set of two out of the six spin-orbital states of the effective $\text{LaAlO}_3/\text{SrTiO}_3$ band model.^[7,61,62] As such, it allows us to study the complex patterns of the Hall signal for every pair of bands individually, without interference from a plethora of additional states. The interplay between the anisotropic d_{yz}/d_{zx} -bands of the 3d t_{2g} orbitals of titanium and the isotropic d_{xy} -band governs the main structure of the Hall signal of the effective six-band model. From this perspective we now concentrate on the Hall conductivity emerging from coupling of an anisotropic ($\mu = 1, t_y^1 = 0.25t_x^1$) and an isotropic ($\mu = 2, t_x^2 = t_y^2 = t_z^2$) cosine band.

Neglecting the energy shift in the effective $\text{LaAlO}_3/\text{SrTiO}_3$ band model due to spacial anisotropy at the interface, these two bands are assumed to be aligned at their bottom. This arrangement leads to a match in energy, and thus filling, of the logarithmic Van Hove singularity of the isotropic band with the upper singularity of the anisotropic band. A two-band model with slightly different relative band positions would be treated analogously.

Two different coupling effects will be considered. A constant coupling term with $\Delta(k_y) = \gamma$ as it arises in the six-band model between the d_{xy} -band and the d_{yz}/d_{zx} -bands due to atomic spin-orbit coupling. Furthermore, a \mathbf{k} -dependent coupling $\Delta(k_y) = -\alpha \sin(k_y)$ is examined. It resembles the coupling term between the d_{xy} -band and the d_{yz}/d_{zx} -bands, introduced by the symmetry breaking at the $\text{LaAlO}_3/\text{SrTiO}_3$ interface.^[61,62]

First, we inspect the Hall conductivity of the two uncoupled bands plotted against the filling factor, as its structure already changes nontrivially with respect to the single-band behavior studied in Section 3.1. The additional structural complexity is caused by the differing densities of states of the two bands. Consequently, the conductivity of the uncoupled two-band system may only be obtained by superposition of the individual signals after a nontrivial transformation of each of them along the filling axis. By color coding the total Hall conductivity (**Figure 6**, purple sections belong to $\mu = 1$, orange sections refer to the orbital contribution $\mu = 2$), the signal is again resolvable from a single-band perspective.

In addition to the asymmetry of the signal with respect to half filling, which results from the alignment of the two bands at their bottom, the most prominent new feature in the Hall conductivity is a step-like descent for fillings between the logarithmic Van Hove singularities. It should not be confused with the similar

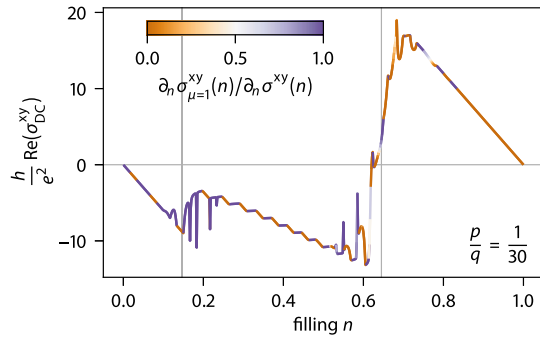


Figure 6. Hall conductivity of an uncoupled two-band model ($\Delta(k_y) = 0$) broken down into distinct band contributions: anisotropic hopping $t_y^1 = 0.25t_x^1$ in the first band ($\mu = 1$) and isotropic hopping $t_x^2 = t_y^2 = t_x^1$ in the second band. The two bands are aligned at their bottom ($\epsilon^\mu = (-1)^\mu 0.75t_x^1$). System size, temperature, and scattering rate are chosen as in Figure 4 and the magnetic flux is at $p/q = 1/30$. Vertical gray lines indicate the positions of logarithmic Van Hove singularities. By calculating the relative change in the Hall signal with filling, coming from state $\mu = 1$ of the field-free model, one obtains the impact of this state on the Hall conductivity at a certain filling factor (see color coding). Loosely speaking, dark purple sections result from the anisotropic band ($\mu = 1$) and dark orange sections are contributions from the isotropic band ($\mu = 2$).

looking quantized Hall conductivity resulting from gaps in the energy spectrum when plotted against the chemical potential. In Figure 6, the signal is shown versus band filling, effectively skipping energy gaps in the dispersion specified by a quantized Hall conductivity.

Thus, the “treads” of those steps cannot be the result of bandgaps. Instead, they are the Hall signal of the wider Hofstadter bands of the anisotropic cosine band, which has open semiclassical orbits in this range of filling, leading to a nearly suppressed transversal conductivity.

The narrow energy gaps between those wider Hofstadter bands manifest themselves in Figure 6 as narrow “topological peaks” interrupting the horizontal progression of the step treads. However, as seen in the single-band case in Section 3.1, they are quickly washed out by scattering and temperature, remaining only visible in the vicinity of the logarithmic Van Hove singularities.

The step “risers”, on the other hand, can be traced back to the flat Hofstadter bands of the isotropic cosine band, corresponding to closed semiclassical orbits. Typically, such a flat Hofstadter band (with $\mu = 2$) is placed energetically somewhere within a wider one (with $\mu = 1$). When the chemical potential reaches this flat Hofstadter band its much higher density of states leads to a near total suspension of the filling up of the wider band, until no empty states are left in the flat band. Thus, the slope of the Hall conductivity changes abruptly compared with the step treads and the height of the riser assumes a nearly quantized value (of e^2/h).

The regime with the step-like behavior is then expected to be heavily affected already by adding a weak coupling term $\Delta(k_y)$ to the Hamiltonian (Figure 7), as the different Hofstadter bands will hybridize strongest at their intersection lines. In the case of a weak magnetic field (Figure 7b), it is actually the only range

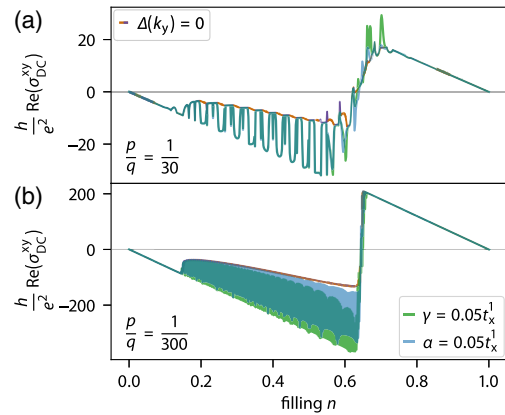


Figure 7. Evolution of the Hall conductivity for a hybridized two-band model: a) Hall signal from Figure 6 ($\Delta(k_y) = 0$) compared with the two different types of band coupling $\Delta(k_y) = \gamma$ and $\Delta(k_y) = -\alpha \sin(k_y)$ for small coupling constants. b) Same as (a) but with a reduced magnetic field.

of filling where the Hall signal of the weakly coupled bands differs significantly from the one of the uncoupled bands. It is striking that a weak perturbation modifies the Hall signal qualitatively—an observation that will be explained below. The other affected region around the coinciding logarithmic Van Hove singularities (Figure 7a), where the Hall signal switches its sign, will not be investigated closer, as it shrinks to zero width in the low magnetic field limit.

For weak coupling strengths, the deviation from the behavior of the uncoupled bands in the step-like region can be well understood by first looking at higher magnetic fields (Figure 8). Band structure and Berry curvature are for weak coupling only

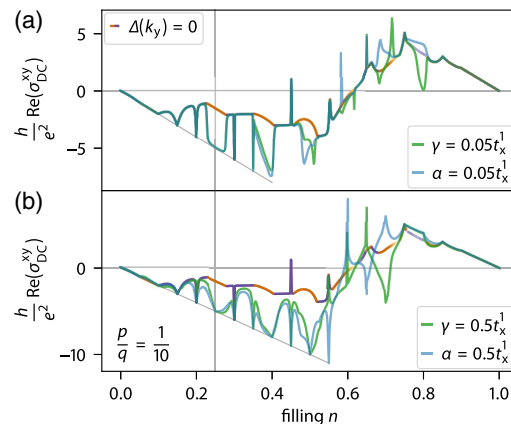


Figure 8. Reappearance of a topologically quantized Hall conductivity for hybridized Hofstadter bands: Hall signal for the uncoupled model of Figure 6 ($\Delta(k_y) = 0$) with an increased magnetic flux of $p/q = 1/10$ compared with the two different types of band coupling $\Delta(k_y) = \gamma$ and $\Delta(k_y) = -\alpha \sin(k_y)$ for a) weak and b) strong coupling. The filling of half an electron per unit cell ($n = 0.25$) is marked by a vertical gray line. For the lower fillings, the integer topological values of the Hall signal line up (descending gray line), as there the magnetic Bloch bands all have a Chern number of +1.

distorted in the vicinity of the former band crossings. So the Hall signal is expected to stay mostly unchanged. It can only deviate significantly from that of uncoupled bands in the filling ranges of the step risers (e.g., $0.2 < n < 0.3$, in Figure 8a).

For a flat primary Hofstadter band intersecting a wider one, the shape of the Hall signal of the hybridized bands can be constructed based on two facts: band repulsion and the Chern numbers of the hybridized magnetic Bloch bands. By hybridization, the wider primary Hofstadter band is split apart at the energy of the flat band and each part is merged with half of the flat band, which is itself split along the intersection lines. Thus forming two new nonintersecting hybridized magnetic Bloch bands.

For weak coupling strengths, the new bands in the regions around the former crossings are pushed above/below the energy of the primary flat Hofstadter band, due to band repulsion. In contrast, in the other regions of the BZ, the band dispersions and also the Berry curvatures are nearly unchanged. This means that filling-wise the progression of the transversal conductivity only changes at the two edges of the former step riser, whereas in the middle part of that region one still finds the same linear trend as before.

For strong coupling, all hybridized magnetic Bloch bands in this regime are energetically separated from each other by finite bandgaps. A Chern number of +1 can in this case easily be read off from Figure 8b for each of the new bands (see the peaks at fillings of completely filled magnetic Bloch bands lined up along a descending line). This must also hold true for the weak coupling case, assuming the bands do not cross while reducing the coupling strength—albeit the hybridized bands may eventually overlap if the flatter band has a finite width.

Somewhere in the middle of the former step riser the energetically lower one of the two hybridized magnetic Bloch bands is completely filled. Assuming energetically nonoverlapping bands or, equivalently, that the upper hybridized band only contributes linearly up to this filling factor, the Hall signal must thus already be shifted down to the descending gray line connecting the integer topological values in Figure 8a. Otherwise, the Chern numbers of the nonintersecting hybridized bands could not be matched correctly. This leads to a broad dip replacing the step riser. It is the separation of the bands due to the hybridization that causes this sizable finite down shift of the Hall signal.

Inspecting the case of a slightly weaker magnetic field more thoroughly (Figure 7), where the assumption of totally flat primary Hofstadter bands is even more accurate, one sees that such a broad dip appears at every former step riser. Thereby replacing the step-like descent by an oscillatory behavior, varying between the signal of the uncoupled bands and the “topological limit”. The gaps between the wider Hofstadter bands, associated with the anisotropic cosine band, must have also been slightly enlarged by the band coupling. In particular one can now identify their narrow peaks in the whole region between the logarithmic Van Hove singularities (Figure 7a), where they were suppressed before by finite temperature and scattering.

For higher temperatures, the energy broadening of $k_B T$ will eventually extend over the range of several magnetic Bloch bands. This then leads to an averaging out of these oscillations. Lowering the magnetic field has the same effect with the addition that new phenomena can arise due to a finite coupling strength, which can then also depend on the specific form of $\Delta(k_y)$.

4. Conclusion

We discussed 2D magnetotransport in the presence of spin–orbit coupling in single-band systems with disorder as well as multiband systems in the clean limit.

Experimentally, we extracted self-consistently both WAL and EEI contributions emerging as first-order quantum corrections to the electrical transport properties of thin BaPbO₃ films. Thus, we offer a consistent way to interpret quantum corrections on 2D films to thoroughly identify an electronically correlated and insulating low-temperature state.

Furthermore, going from a single-band system to a general multiband setup, we investigated a defect-free lattice system which reveals a striking behavior when electronic bands hybridize in the presence of a magnetic field. We first reanalyzed the Hall conductivity of the anisotropic Hofstadter model, where open semiclassical orbits lead to a deviation from the well-known linear behavior in the electron density of closed orbits. This fundamental knowledge of the single-band behavior of the conductivity then allowed us to fully understand an uncoupled multiband system. The additional effects of a weak band coupling in this multiband system can be explained by the hybridization of intersecting Hofstadter bands instead of the field-free bands.

Hereafter, it would be intriguing to investigate a disordered system in a generic multiband setup to merge the aspects investigated in our complementary studies. The implementation of band hybridization into a generalized version of the Iordanskii–Lyanda-Geller–Pikus theory will be challenging but allows for a fundamental understanding of multiband quantum interference.

Acknowledgements

R.B. and E.L. contributed equally to this work. Financial support by the Deutsche Forschungsgemeinschaft (project number 107745057, TRR 80) is gratefully acknowledged.

Open Access funding enabled and organized by Projekt DEAL.

Conflict of Interest

The authors declare no conflict of interest.

Data Availability Statement

Research data are not shared.

Keywords

Hofstadter bands, magnetotransport, multiband, oxide heterostructures, spin–orbit coupling, 2D, weak antilocalization

Received: April 15, 2021

Revised: September 7, 2021

Published online: October 5, 2021

- [1] P. Zubko, S. Gariglio, M. Gabay, P. Ghosez, J.-M. Triscone, *Annu. Rev. Condens. Matter Phys.* **2011**, 2, 141.
- [2] H. Y. Hwang, Y. Iwasa, M. Kawasaki, B. Keimer, N. Nagaosa, Y. Tokura, *Nat. Mater.* **2012**, 11, 103.
- [3] J. Mannhart, D. G. Schlom, *Science* **2010**, 327, 1607.
- [4] R. Hesper, L. H. Tjeng, A. Heeres, G. A. Sawatzky, *Phys. Rev. B* **2000**, 62, 16046.
- [5] S. Okamoto, A. J. Millis, *Nature* **2004**, 428, 630.
- [6] P. Seiler, J. Zabaleta, R. Wanke, J. Mannhart, T. Kopp, D. Braak, *Phys. Rev. B* **2018**, 97, 075136.
- [7] Y. Kim, R. M. Lutchyn, C. Nayak, *Phys. Rev. B* **2013**, 87, 245121.
- [8] P. Seiler, R. Bartel, T. Kopp, G. Hammerl, *Phys. Rev. B* **2019**, 100, 165402.
- [9] M. Liu, C.-Z. Chang, Z. Zhang, Y. Zhang, W. Ruan, K. He, L.-l. Wang, X. Chen, J.-F. Jia, S.-C. Zhang, Q.-K. Xue, X. Ma, Y. Wang, *Phys. Rev. B* **2011**, 83, 165440.
- [10] J. Wang, A. M. DaSilva, C.-Z. Chang, K. He, J. K. Jain, N. Samarth, X.-C. Ma, Q.-K. Xue, M. H. W. Chan, *Phys. Rev. B* **2011**, 83, 245438.
- [11] E. P. Amaladass, T. R. Devidas, S. Sharma, A. Mani, *J. Phys.: Condens. Matter* **2017**, 29, 175602.
- [12] H.-Z. Lu, S.-Q. Shen, *Phys. Rev. B* **2011**, 84, 125138.
- [13] P. W. Anderson, *Phys. Rev.* **1958**, 109, 1492.
- [14] E. Abrahams, P. W. Anderson, D. C. Licciardello, T. V. Ramakrishnan, *Phys. Rev. Lett.* **1979**, 42, 673.
- [15] S. Hikami, A. I. Larkin, Y. Nagaoka, *Prog. Theor. Phys.* **1980**, 63, 707.
- [16] B. L. Altshuler, A. G. Aronov, P. A. Lee, *Phys. Rev. Lett.* **1980**, 44, 1288.
- [17] P. A. Lee, T. V. Ramakrishnan, *Rev. Mod. Phys.* **1985**, 57, 287.
- [18] G. Bergmann, *Phys. Rep.* **1984**, 107, 1.
- [19] S. V. Iordanskii, Y. B. Lyanda-Geller, G. E. Pikus, *JETP Lett.* **1994**, 60, 199.
- [20] M. I. D'yakonov, V. Perel', *Sov. Phys. Solid State* **1972**, 13, 3023.
- [21] W. Knap, C. Skierbiszewski, A. Zduniak, E. Litwin-Staszewska, D. Bertho, F. Kobbi, J. L. Robert, G. E. Pikus, F. G. Pikus, S. V. Iordanskii, V. Mosser, K. Zekentes, Y. B. Lyanda-Geller, *Phys. Rev. B* **1996**, 53, 3912.
- [22] F. G. Pikus, G. E. Pikus, *Phys. Rev. B* **1995**, 51, 16928.
- [23] Y.-Y. Pai, A. Tylan-Tyler, P. Irvin, J. Levy, *Rep. Prog. Phys.* **2018**, 81, 036503.
- [24] H. Nakamura, T. Koga, T. Kimura, *Phys. Rev. Lett.* **2012**, 108, 206601.
- [25] P. Seiler, Ph.D. thesis, Universität Augsburg, Augsburg, **2018**.
- [26] P. D. Dresselhaus, C. M. A. Papavassiliou, R. G. Wheeler, R. N. Sacks, *Phys. Rev. Lett.* **1992**, 68, 106.
- [27] J. J. Lin, J. P. Bird, *J. Phys.: Condens. Matter* **2002**, 14, R501.
- [28] E. Abrahams, P. W. Anderson, P. A. Lee, T. V. Ramakrishnan, *Phys. Rev. B* **1981**, 24, 6783.
- [29] B. L. Altshuler, D. Khmel'nitzkii, A. I. Larkin, P. A. Lee, *Phys. Rev. B* **1980**, 22, 5142.
- [30] M. Kawasaki, K. Takahashi, T. Maeda, R. Tsuchiya, M. Shinohara, O. Ishiyama, T. Yonezawa, M. Yoshimoto, H. Koinuma, *Science* **1994**, 266, 1540.
- [31] G. Koster, B. L. Kropman, G. J. H. M. Rijnders, D. H. A. Blank, H. Rogalla, *Appl. Phys. Lett.* **1998**, 73, 2920.
- [32] D. Fuchs, A. Sleem, R. Schäfer, A. G. Zaitsev, M. Meffert, D. Gerthsen, R. Schneider, H. v. Löhneysen, *Phys. Rev. B* **2015**, 92, 155313.
- [33] A. Carl, G. Dumpich, D. Hallfarth, *Phys. Rev. B* **1989**, 39, 3015.
- [34] P. Seiler, E. Lettl, D. Braak, T. Kopp, *Phys. Rev. B* **2019**, 100, 121404.
- [35] P. Seiler, E. Lettl, D. Braak, T. Kopp, *Phys. Rev. B* **2019**, 100, 115415.
- [36] R. Kubo, *J. Phys. Soc. Jpn.* **1957**, 12, 570.
- [37] G. D. Mahan, *Many-Particle Physics*, Physics of Solids and Liquids, 3rd ed., Springer US, Boston, MA **2000**.
- [38] P. B. Allen, in *Contemporary Concepts of Condensed Matter Science*, Volume 2 of Conceptual Foundations of Materials (Eds: S. G. Louie, M. L. Cohen), Elsevier, Amsterdam **2006**, Ch. 6.
- [39] T. B. Boykin, *Phys. Rev. B* **1995**, 52, 16317.
- [40] J. M. Tomczak, S. Biermann, *Phys. Rev. B* **2009**, 80, 085117.
- [41] T. B. Boykin, M. Luisier, G. Klimeck, *Eur. J. Phys.* **2010**, 31, 1077.
- [42] R. Peierls, *Z. Phys.* **1933**, 80, 763.
- [43] J. M. Luttinger, *Phys. Rev.* **1951**, 84, 814.
- [44] B. A. Foreman, *Phys. Rev. B* **2002**, 66, 165212.
- [45] T. B. Boykin, M. Luisier, M. Salmani-Jelodar, G. Klimeck, *Phys. Rev. B* **2010**, 81, 125202.
- [46] J. Zak, *Phys. Rev.* **1964**, 134, A1602.
- [47] J. Zak, *Phys. Rev.* **1964**, 134, A1607.
- [48] E. Brown, *Phys. Rev.* **1964**, 133, A1038.
- [49] D. R. Hofstadter, *Phys. Rev. B* **1976**, 14, 2239.
- [50] M.-C. Chang, Q. Niu, *Phys. Rev. B* **1996**, 53, 7010.
- [51] M. Arai, Y. Hatsugai, *J. Phys.: Conf. Ser.* **2011**, 334, 012042.
- [52] S. Mugel, A. Dauphin, P. Massignan, L. Tarruell, M. Lewenstein, C. Lobo, A. Celi, *SciPost Phys.* **2017**, 3, 012.
- [53] P. G. Harper, *Proc. Phys. Soc. A* **1955**, 68, 874.
- [54] B. A. Bernevig, *Topological Insulators and Topological Superconductors*, Princeton University Press, Princeton **2013**.
- [55] D. J. Thouless, M. Kohmoto, M. P. Nightingale, M. den Nijs, *Phys. Rev. Lett.* **1982**, 49, 405.
- [56] B. Göbel, A. Mook, J. Henk, I. Mertig, *Phys. Status Solidi B* **2020**, 257, 1900518.
- [57] L. Van Hove, *Phys. Rev.* **1953**, 89, 1189.
- [58] M. Arai, Y. Hatsugai, *Physica E* **2010**, 42, 740.
- [59] M. Y. Azbel, P. Bak, P. M. Chaikin, *Phys. Rev. Lett.* **1987**, 59, 926.
- [60] N. W. Ashcroft, N. D. Mermin, *Solid State Physics*, Holt, Rinehart and Winston, New York **1976**.
- [61] G. Khalsa, B. Lee, A. H. MacDonald, *Phys. Rev. B* **2013**, 88, 041302.
- [62] Z. Zhong, A. Tóth, K. Held, *Phys. Rev. B* **2013**, 87, 161102.